Scientia Iranica (2024) 31(1), 1–14

Sharif University of Technology
**Scientia Iranica**
*Transactions B: Mechanical Engineering*
https://scientiairanica.sharif.edu

# Mechanical design of a 5-DOF robotic interface for application in haptic simulation systems of large-organ laparoscopic surgery

**H. Jamshidifar[a,b], F. Farahmand[a,*], S. Behzadipour[a], and A. Mirbagheri[c]**

a. *Department of Mechanical Engineering, Sharif University of Technology, Tehran, Iran.*
b. *Robotic Surgery Lab., RCBTR, Tehran University of Medical Sciences, Tehran, Iran.*
c. *Department of Medical Physics & Biomedical Eng., School of Medicine, Robotic Surgery Lab., RCBTR, Tehran University of Medical Sciences, Tehran, Iran.*

Received 17 July 2021; received in revised form 3 November 2022; accepted 5 April 2023

**KEYWORDS**
Conceptual design;
Kinematics analysis;
Design synthesis;
Workspace;
Motion tracking.

**Abstract.** Laparoscopic manipulation of delicate large intra-abdominal organs is a difficult task that needs special training programs to improve the surgeons' dexterity. In this study, the mechanical design of a robotic interface for haptic simulation of large-organ laparoscopic surgery is described. The designed robot enjoys five active Degree of Freedoms (DOFs), back drivability, low inertia, friction and backlash, and sufficiently large force/moment production capacity. The kinematics of the robot was analyzed and a functional prototype was fabricated for experimental tests. Results indicated that the target workspace was fully covered with no singular points inside. The mechanism was highly isotropic and the torque requirements were in the acceptable range. The trajectory tracking experiments against a 1 kg payload revealed an Root Mean Square (RMS) of 0.9 mm, due to the simplifications of the kinematic model, i.e., not considering the friction and backlash effects. It was concluded that the designed robot could satisfy the mechanical requirements for being used as the robotic interface in a haptic large-organ laparoscopic surgery simulation system.



## 1. Introduction

Laparoscopic surgery, as a minimally invasive procedure, involves less operative trauma and post-surgical complications for the patient, reducing the time and cost of hospitalization. However, it is a difficult job for surgeons due to the loss of direct visual and tactile information. The 2-D images, provided by the laparoscopic camera, do not contain the depth information needed for effective manipulation of body organs. Furthermore, the long narrow instruments of laparoscopic surgery have limited maneuverability and cause a fulcrum effect around their insertion points as the tool's tip moves in the opposite direction of the surgeon's hand [1]. These difficulties are more critical when dealing with delicate large intra-abdominal organs such as the spleen, bowel, and liver [2–6].

In order to be prepared for the complex gestures and the hand-eye coordination skills needed during surgery; laparoscopic surgery trainees require special training programs. The traditional approach is to practice the surgical procedure on animal models; this

*. *Corresponding author. Tel.: +98 21 66165532; Fax: +98 21 66000021*
*E-mail addresses: hamed_jamshidifar@alum.sharif.edu (H. Jamshidifar); farahmand@sharif.edu (F. Farahmand); behzadipour@sharif.edu (S. Behzadipour); a-mirbagheri@tums.ac.ir (A. Mirbagheri)*

doi: 10.24200/sci.2023.58723.5866

is restricted, however, by the fact that it needs special animal lab facilities and cannot be practiced repetitively due to ethical and economic problems [7]. An alternative approach, that has gained much attention in recent years, is to use of surgical simulation systems. These systems replicate the real surgery conditions within a virtual environment, enabling the trainees to repeat a procedure unlimitedly and experience complicated situations [1,7,8]. The two main components of a laparoscopy surgical simulation system are: 1) an interactive graphical environment of the surgery site that involves a deformable model of the soft tissues, and 2) a robotic interface, preferably with force feedback capability, between the surgeon's hand and the virtual environment [9]. The robotic interface of a haptic simulator of laparoscopic surgery is in fact a dummy surgical tool that receives the surgeon's hand motions, to be transferred to the graphical environment, and uses the tool-tissue force interaction data from the deformable model, to mimic the mechanical interactions between the surgeon's hand and the surgical tool.

A number of different robotic interfaces have been introduced to be used in haptic laparoscopic surgery simulation systems. Some researchers have attempted to utilize general-purpose haptic devices which are commercially available, e.g. PHANToM OMNI (Immersion, Bordeaux, France) [10]. However, such systems are not customized for laparoscopic surgery and suffer from redundant, irrelevant, or insufficient Degree of Freedoms (DOFs), incompatible workspace and kinematical constraints, and inappropriate force and torque-producing capabilities [8,11]. In another line of work, researchers have developed specially designed robotic interfaces, based on the actual DOFs and other functional characteristics of laparoscopic surgery [12–14]. In spite of their reasonable efficacy, such systems can cover only a limited range of laparoscopic surgery operations. In particular, none of the previously designed robotic interfaces is capable of being used for the simulation of large intra-abdominal organ surgeries. This is while it is quite a difficult task to manipulate these organs safely and securely using the available fan retractors and long-jaw graspers [15–20] On one side, the tiny laparoscopic instruments are incapable of grasping a sufficiently large part of the organ to fully constrain it [3,21,22]. On the other side, the application of large forces to prevent slippages may be injurious for such tissues, e.g., spleen, liver, kidney, and urinary bladder, which are often delicate and vulnerable to damage [4,23–26].

For a haptic surgical simulation system to be used for training large organs grasping/retraction, the robotic interface needs to be exclusively designed. The system should have an active fifth DOF, in addition to the yaw-pitch-roll and insertion DOFs of the commonly available devices, to reproduce the force interactions between the tool jaws and the organ. Considering the critical role of this force in the safe and secure manipulation of large delicate organs, it is particularly important that this DOF has high transparency in force reflection. Moreover, the magnitudes of interaction forces/moments produced during laparoscopic surgery of large organs are substantially higher than small organs, due to their larger mass and inertia and stronger ligamentous connections [4,21,23]. As a result, the robot needs to be equipped with sufficiently high-capacity actuators at all DOFs. This is particularly true for the roll DOF which often experiences much higher interaction torques during large organ surgery, in comparison with small tissue surgery, due to longer tool jaws [21]. The necessity of using larger and heavier actuators raises new concerns in the design of the system, considering the fact that they need to be mounted at stationary positions or in a counterbalanced configuration to reduce the inertial and/or weight effects. Furthermore, large interaction forces/moments may result in higher friction and backlash effects in the system that would disturb its transparency in force reflection.This paper describes and evaluates the mechanical design of a new 5-DOF robotic interface for application in haptic simulation systems of laparoscopic surgery, to be used for training of safe and secure grasping/retraction of large intra-abdominal organs. A mechanism, based on the gimbal parallel four-bar linkage, is designed and integrated with three serial joints in series, to provide the required workspace and DOFs, i.e., yaw, pitch, roll, insertion, and grasping. The actuators are located stationary, for the yaw and pitch DOFs, or in a counterbalanced configuration, for the roll and insertion DOFs, with cable-driven transmissions to reduce the inertial, friction, and backlash effects. With such a novel configuration, the designed robot enjoys a much larger payload capacity in all 5 DOFs compared to similar robots, which is critical for providing a realistic haptic sense in the surgeon's hands during laparoscopic surgery simulation of large organs. The efficacy of the designed system for being used as the robotic interface of a large organ grasping simulator is then evaluated experimentally.

## 2. Materials and methods

### *2.1. Conceptual design*

The main functional requirements in designing a robotic interface for haptic simulation systems of laparoscopic surgery include appropriate and sufficient DOFs and workspace, to allow for reproducing the motion of the laparoscopic tool around and into the incision entry, and adequate force/moment production capacity, to enable reconstruction of the tool-tissue interactions in the surgeon's hand. A laparoscopic surgical tool has four DOFs due to the kinematical

constraints imposed by the incision entry, i.e., three rotations about the incision point (pitch, yaw, and roll) and one insertion along the tool. The grasping motion of the thumb, which enables the actuation of the tool's tip, forms a fifth DOFs. The desired range of motion for each of these DOFs is indicated in Table 1, using the records in the literature [27]. Figure 1 illustrates the resulting workspace for the tool's tip.

The force/moment interactions of the tool and body include those occurring between the tool's tip and the operating organ, and those happening between the tool shaft and the abdominal wall at the incision point. The latter effects are insignificant in comparison with the first ones and might be reasonably ignored. The force/moment interactions between the tool handle and the surgeon's hand, shown with dashed lines in Figure 2, correspond with those between the tool's tip and the organ. They include three perpendicular forces, i.e., $f_{hx}$, $f_{hy}$, and $f_{hz}$, a torsional moment around the tool shaft, i.e., $m_{hz}$, and a bending moment which is the result of the thumb's grasping force, i.e., $m_{hg}$. The maximum magnitudes of these forces and moments, as reported in the literature [28,29], indicate the required force/moment production capacity for each DOF of the robotic interface of a large organ surgical simulation system.

In addition to the functional requirements indicated in Table 1, low friction and moving inertia, high structural stiffness, and static balance and back drivability are some of the other requirements that should be considered in the design of any robotic interface for haptic simulation systems, to ensure high transparency in force reflection.

**Table 1.** The range of motion and force/moment production requirements for the robotic interface of a haptic simulator of large organ laparoscopic surgery.

| DOF | Range | Torque/force |
|---|---|---|
| Pitch | 120° | 5 Nm |
| Yaw | 120° | 5 Nm |
| Insertion | 200 mm | 30 N |
| Roll | 280° | 1 Nm |
| Handle grasping | 20° | 15 N |

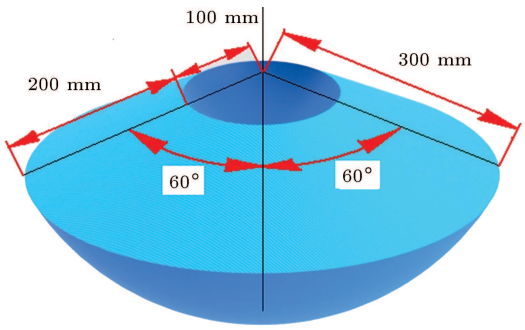


**Figure 1.** The desired workspace of the tool's tip.

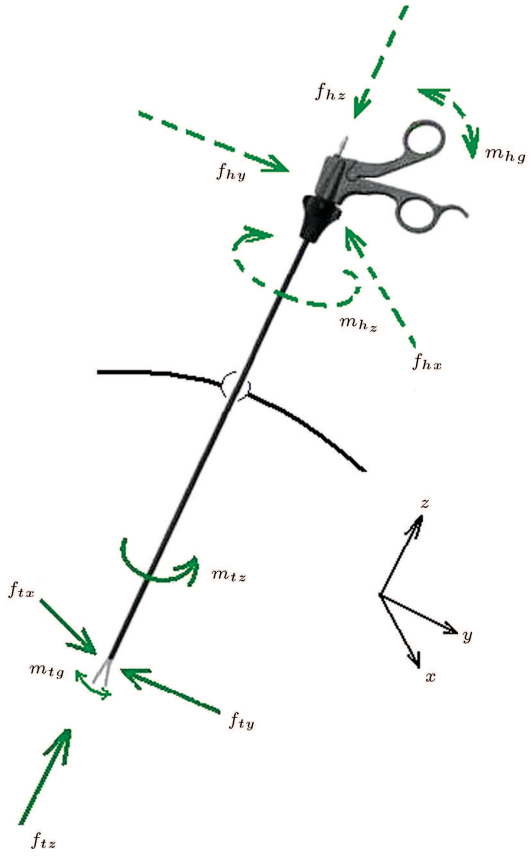


**Figure 2.** Force/moment interactions between the tool and organ (continuous lines), and the tool and surgeon's hand (dashed lines). $f_{tx}$, $f_{ty}$, $f_{tz}$, and $m_{tg}$ are the force components and the resultant moment at the tool's tip, and $m_{tz}$ is the torsion around the tool shaft, all resulting from tool-organ interactions. The corresponding force/moment interactions at the surgeon's hand are represented by $f_{hx}$, $f_{hy}$, and $f_{hz}$, as three force components, $m_{hz}$, as a torsional moment around the tool shaft, and $m_{hg}$, as the resultant moment of the thumb's grasping force.

The proposed mechanism is based on a parallel four-bar linkage, with appropriate modifications to satisfy the above-mentioned requirements. The classical gimbal parallel four-bar linkage mechanism is integrated with three serial joints in series, to form a hybrid design with five DOFs (Figure 3). Two rotational DOFs of the tool shaft about the yaw and pitch axes, i.e., joint variables $q_1$ and $q_2$ in Figure 3, respectively, are provided by the parallel four-bar linkage mechanism. A rolling/linear bearing attached to the gimbal at the intersection of the pitch and yaw axes provides the rolling and translational DOFs of the tool shaft, i.e., joint variables $q_3$ and $q_4$ in Figure 3, respectively. Finally, a grasping DOF is incorporated into the tool handle to provide the fifth DOF, i.e., joint variable $q_5$ in Figure 3.

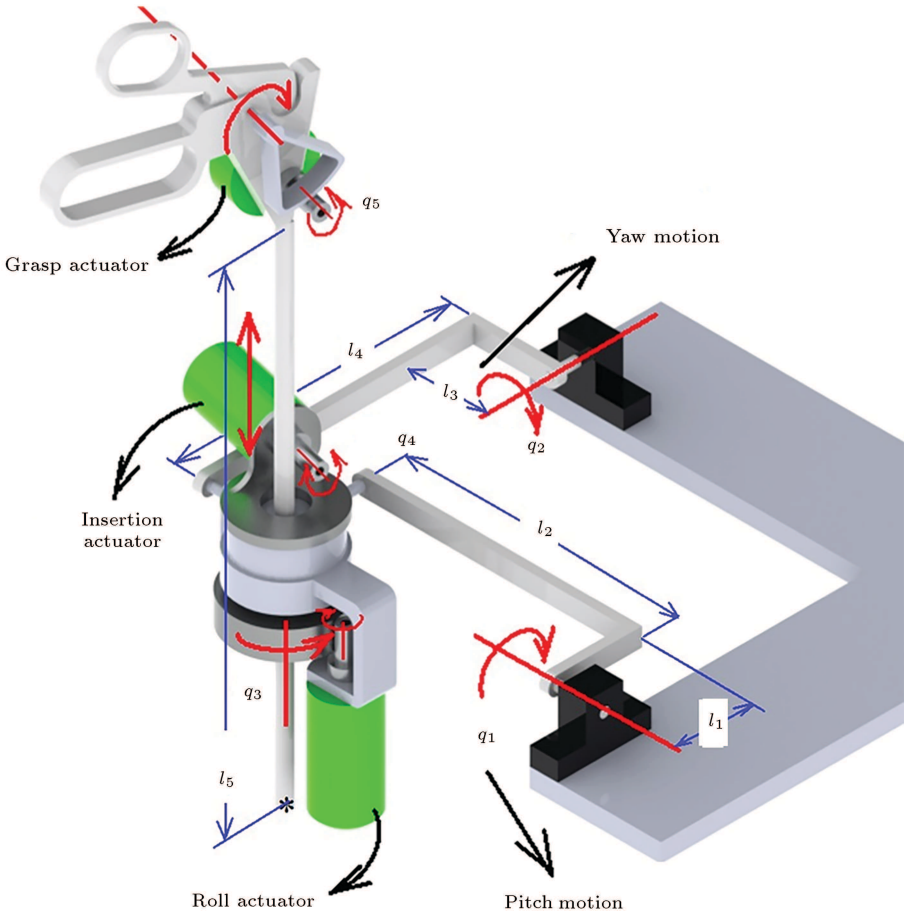


**Figure 3.** A schematic view of the robotic interface of the haptic simulator of large organ grasping. The main design parameters of the robot are shown in the figure.

The proposed mechanism has a fixed point at the intersection of the yaw and pitch axes (center of the gimbal), through which the roll and insertion axes pass. The actuators of the mechanism are mounted on the structure so that their moving inertia is minimized. As illustrated in Figure 3, the actuators of the pitch and yaw DOFs are stationary and the actuators of the linear and roll DOFs are located as close as possible to the fixed center of the mechanism. The only moving actuator located at a distance from the center is that of the grasping DOF. However, due to the small size of this actuator, its moving inertia has a small impact on the overall inertia of the mechanism.

### *2.2. Kinematics analysis*

A detailed kinematics analysis was performed on the proposed mechanism to identify its important design parameters (Figure 3) and evaluate its performance. Assuming the tool handle is the end-effecter, its orientation and location might be described by $\theta_1$, $\alpha$, $l$, and $\gamma$ as the coordinate variables (Figure 4(a)). $\theta_1$ denotes the pitch angle of the $x_1y_1z_1$ coordinate system, fixed to link 1, about the $x$ axis, with respect to the base frame. $\alpha$ represents the yaw angle of the $x_3y_3z_3$ coordinate system, fixed to link 3 at the center point of the mechanism, about the $y$ axis, with respect to frame 1. Finally, $l$ and $\gamma$ are defined using the $x_5y_5z_5$ coordinate system fixed to link 5. The linear distance, $l$, is the displacement of frame 5 along $z_5$, and $\gamma$ is the roll angle of frame 5 around $z_5$, both with respect to frame 3. In brief, $\theta_1$, $\alpha$, and $\gamma$ are the Euler angles, in $x_1y_3z_5$ order, which results in the final orientation of the tool shaft. Thus, the rotation matrix of $\mathbf{R}_5^0$ may be expressed as:

$$\mathbf{R}_5^0 = \mathbf{R}_x(\theta_1)\,\mathbf{R}_y(\alpha)\,\mathbf{R}_z(\gamma). \tag{1}$$

In forward kinematics analysis, we look for the end-effector coordinates, i.e., $\theta_1$, $\alpha$, $l$, and $\gamma$, having the joint variables $q_1$ to $q_4$. Considering Figures 3 and 4(a), this relationship is linear and simple for $\theta_1$, $l$, and $\gamma$:

$$\begin{aligned} \theta_1 &= q_1, \\ l &= r \cdot q_4, \\ \gamma &= q_3, \end{aligned} \tag{2}$$

where $r$ is the transmission ratio which converts the angular velocity of the insertion actuator to the linear

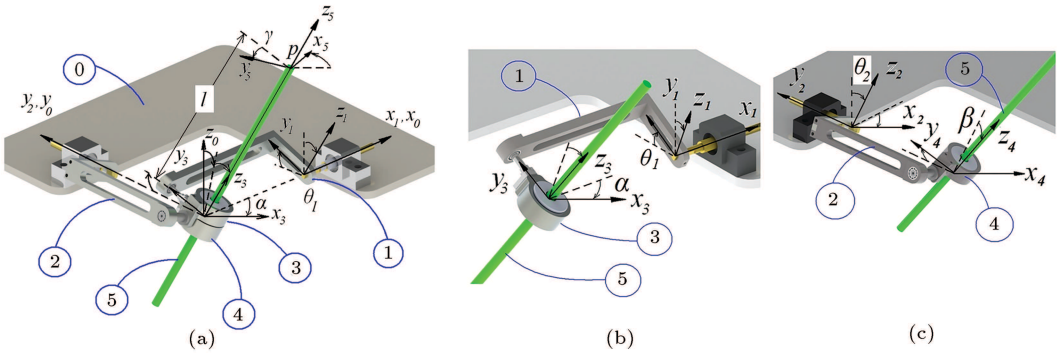


**Figure 4.** Schematic representations of the robot's linkage system to illustrate: (a) the relationships between the kinematical variables in an arbitrary orientation of the tool shaft, (b) the effects of $\theta_1$ and $\alpha$ on the orientation of the tool shaft, (c) the effects of $\theta_2$ and $\beta$ on the orientation of the tool shaft. The links of the mechanism are denoted by (0) for the base frame, (1 & 2) for the gimbal arms, (3 & 4) for the rolling/sliding bearing at the center of the gimbal, and (5) for the tool shaft.

velocity of the tool shaft (see Figure 3).

The single coordinate which has a nonlinear relationship with the joint angles is $\alpha$. Here we obtain an explicit solution for $\alpha$ in order to minimize the computational cost of the kinematics analysis. As mentioned in the frame definitions above and also illustrated in Figure 4(a), $y_3$ and $y_1$ are parallel or in other words, $\hat{\mathbf{e}}_{y_3}$ and $\hat{\mathbf{e}}_{y_1}$ are equal. The rotation of $x_3y_3z_3$ around its $y$ axis generates $\alpha$ as the yaw angle of link 3. Thus $\alpha$ might be found by the inner product of $\hat{\mathbf{e}}_{x_3}$ and $\hat{\mathbf{e}}_{x_1}$. The unit vector $\hat{\mathbf{e}}_{x_1}$ is equal to $\hat{\mathbf{e}}_{x_0}$ and hence available. In order to find $\hat{\mathbf{e}}_{x_3}$, we can use the cross product of $\hat{\mathbf{e}}_{y_3}$ and $\hat{\mathbf{e}}_{z_3}$, if $\hat{\mathbf{e}}_{z_3}$ is known. To obtain the unit vector $\hat{\mathbf{e}}_{z_3}$ we used two expressions for the tool shaft orientation and set them equal. The first expression was based on the relationship between the $x_1y_1z_1$ and $x_3y_3z_3$ coordinate systems (Figure 4(b)), which provided the tool shaft orientation, $\hat{\mathbf{e}}_{z_3}$, using $\theta_1$ and $\alpha$. The second expression was based on the angles of the other arm of the mechanism (Figure 4(c)). Assuming $x_2y_2z_2$ and $x_4y_4z_4$ as the coordinate systems fixed to links 2 and 4, respectively, the tool shaft orientation, $\hat{\mathbf{e}}_{z_4}$, was determined using $\theta_2$ and $\beta$, as the yaw angles of these coordinate systems. Since the tool orientation is the same, $\hat{\mathbf{e}}_{z_3}$ and $\hat{\mathbf{e}}_{z_4}$ are equal. Thus:

$$\hat{\mathbf{e}}_{z_3} = \hat{\mathbf{e}}_{z_4} = \frac{\hat{\mathbf{e}}_{x_4} \times \hat{\mathbf{e}}_{y_3}}{|\hat{\mathbf{e}}_{x_4} \times \hat{\mathbf{e}}_{y_3}|} = \frac{\hat{\mathbf{e}}_{x_2} \times \hat{\mathbf{e}}_{y_1}}{|\hat{\mathbf{e}}_{x_2} \times \hat{\mathbf{e}}_{y_1}|}. \tag{3}$$

By replacing $\hat{\mathbf{e}}_{y_1}$ and $\hat{\mathbf{e}}_{x_2}$ in Eq. (3), $\hat{\mathbf{e}}_{z_3}$ is found as:

$$\hat{\mathbf{e}}_{z_3} = \frac{1}{(c_1^2 s_2^2 + c_2^2)^{1/2}} \begin{pmatrix} c_2 \\ 0 \\ -s_2 \end{pmatrix} \times \begin{pmatrix} 0 \\ c_1 \\ s_1 \end{pmatrix} = \begin{pmatrix} \frac{c_1 s_2}{(c_1^2 s_2^2 + c_2^2)^{1/2}} \\ \frac{-s_1 c_2}{(c_1^2 s_2^2 + c_2^2)^{1/2}} \\ \frac{c_1 c_2}{(c_1^2 s_2^2 + c_2^2)^{1/2}} \end{pmatrix}, \tag{4}$$

where $s_i$ is $\sin(\theta_i)$, and $c_i$ is $\cos(\theta_i)$. In order to find $\hat{\mathbf{e}}_{x_3}$, we use the cross product of $\hat{\mathbf{e}}_{z_3}$ and $\hat{\mathbf{e}}_{y_3}$:

$$\hat{\mathbf{e}}_{x_3} = \begin{pmatrix} 0 \\ c_1 \\ s_1 \end{pmatrix} \times \begin{pmatrix} \frac{c_1 s_2}{(c_1^2 s_2^2 + c_2^2)^{1/2}} \\ \frac{-s_1 c_2}{(c_1^2 s_2^2 + c_2^2)^{1/2}} \\ \frac{c_1 c_2}{(c_1^2 s_2^2 + c_2^2)^{1/2}} \end{pmatrix} = \begin{pmatrix} \frac{c_2}{(c_1^2 s_2^2 + c_2^2)^{1/2}} \\ \frac{s_1 s_2 c_1}{(c_1^2 s_2^2 + c_2^2)^{1/2}} \\ \frac{-c_1^2 s_2}{(c_1^2 s_2^2 + c_2^2)^{1/2}} \end{pmatrix}, \tag{5}$$

which allows $\alpha$ to be determined uniquely using Eq. (6):

$$\alpha = \tan^{-1}\left(\frac{\sin(\alpha)}{\cos(\alpha)}\right) = \tan^{-1}\left(\frac{\frac{|\hat{\mathbf{e}}_{x_1} \times \hat{\mathbf{e}}_{x_3}|}{|\hat{\mathbf{e}}_{x_1}| \times |\hat{\mathbf{e}}_{x_3}|}}{\hat{\mathbf{e}}_{x_1} \cdot \hat{\mathbf{e}}_{x_3}}\right) = \tan^{-1}\left(\frac{c_1 s_2}{c_2}\right). \tag{6}$$

Eqs. (2) and (6) provide all entries of the rotation matrix of the tool shaft (Eq. (1)):

$$\mathbf{R}_5^0 = \begin{pmatrix} \frac{c_2 c_3}{\sqrt{e}} & -\frac{c_2 s_3}{\sqrt{e}} & \frac{c_1 s_2}{\sqrt{e}} \\ \frac{s_1 s_2 c_1 c_3}{\sqrt{e}} + c_1 s_3 & -\frac{s_1 s_2 c_1 s_3}{\sqrt{e}} + c_1 c_3 & \frac{-s_1 c_2}{\sqrt{e}} \\ \frac{-c_1^2 s_2 c_3}{\sqrt{e}} + s_1 s_3 & \frac{c_1^2 s_2 s_3}{\sqrt{e}} + s_1 c_3 & \frac{c_1 c_2}{\sqrt{e}} \end{pmatrix}, \tag{7}$$

where $e$ is defined as $e = c_1^2 s_2^2 + c_2^2$.

Having $\mathbf{R}_5^0$, the position of the tool's tip (point $p$ in Figure 4 (a)) can be also found using Eq. (8):

$$\vec{\mathbf{p}} = \begin{pmatrix} x_p \\ y_p \\ z_p \end{pmatrix} = \mathbf{R}_5^0 \begin{pmatrix} 0 \\ 0 \\ l \end{pmatrix} = \begin{pmatrix} l\frac{c_1 s_2}{\sqrt{c_1^2 s_2^2 + c_2^2}} & -l\frac{s_1 c_2}{\sqrt{c_1^2 s_2^2 + c_2^2}} & l\frac{c_1 c_2}{\sqrt{c_1^2 s_2^2 + c_2^2}} \end{pmatrix}^T. \tag{8}$$

The inverse kinematics of the mechanism involves the

equations that provide the joint variables in terms of a given set of coordinate variables for the tool's tip, i.e., $(x_p, y_p, z_p)$. It is clear that the roll of the tool is directly determined by the roll motor and hence the relation is trivial. For other joint variables, we used Eq. (8) to obtain the inverse kinematics equations as in the following:

$$q_1 = \arctan\left(-\frac{y_p}{z_p}\right), \qquad q_2 = \arctan\left(-\frac{x_p}{z_p}\right),$$
$$l = \sqrt{x_p^2 + y_p^2 + z_p^2}. \tag{9}$$

The next step of the kinematics analysis was the velocity analysis, by which the relations between the velocity vector of the tool's tip, i.e., its linear and angular velocities at the four DOFs, and the angular velocities of the joints are determined. The absolute velocity of the tool's tip was expressed by vector $\vec{\mathbf{v}}_5^5 = \left(\omega_x^5, \omega_y^5, \omega_z^5, \dot{l}\right)^T$ which gives the velocity of frame 5 expressed in frame 5 (Figure 4(a)). Expressing the velocity in frame 5 is favorable as it is easily related to the hand velocity and also results in a sensible relationship for deriving the Jacobian matrix. Assuming the joint rates vector to be represented by $\dot{\vec{\mathbf{q}}} = (\dot{q}_1, \dot{q}_2, \dot{q}_3, \dot{q}_4)^T$, we then differentiated the rotation matrix (Eq. (7)) as a common method for finding its components. This allowed finding $\mathbf{S}(\omega)$ as the skew-symmetric matrix of the angular velocity, also known as the angular velocity tensor (18):

$$\frac{d}{dt}(\mathbf{R}_5^0) = \mathbf{S}(\omega)\,\mathbf{R}_5^0, \tag{10}$$

$$\mathbf{S}(\omega) = \frac{d}{dt}(\mathbf{R}_5^0)\,(\mathbf{R}_5^0)^T = \begin{pmatrix} 0 & -\dot{\alpha}s_1 & \dot{\alpha}c_1 \\ \dot{\alpha}s_1 & 0 & -\dot{\theta} \\ -\dot{\alpha}c_1 & \dot{\theta} & 0 \end{pmatrix}. \tag{11}$$

On the other hand, by definition:

$$\mathbf{S}(\omega) = \begin{pmatrix} 0 & -\omega_z^0 & \omega_y^0 \\ \omega_z^0 & 0 & -\omega_x^0 \\ -\omega_y^0 & \omega_x^0 & 0 \end{pmatrix}. \tag{12}$$

Which provided the angular velocity vector of the tool shaft in the base frame and then frame 5 as:

$$\vec{\boldsymbol{\omega}}_{\mathbf{5}}^{\mathbf{0}} = \left(\omega_x^0, \omega_y^0, \omega_z^0\right)^T, \tag{13}$$

$$\vec{\boldsymbol{\omega}}_5^5 = \mathbf{R}_0^5 \vec{\boldsymbol{\omega}}_5^0 = \left(\mathbf{R}_5^0\right)^T \vec{\boldsymbol{\omega}}_5^0. \tag{14}$$

The fourth entry in the absolute velocity vector of the tool's tip was obtained simply by differentiating Eq. (2). Thus, the Jacobian matrix of the mechanism, which relates the velocity of the tool's tip and the joint rates, was determined as:

$$\mathbf{J}(q) = \begin{pmatrix} \frac{c_3c_2}{\sqrt{e}} - \frac{s_1s_2s_3c_2}{e} & \frac{s_3c_1}{e} & 0 & 0 \\ -\frac{s_3c_2}{\sqrt{e}} - \frac{c_3c_2s_1s_2}{e} & \frac{c_3c_1}{e} & 0 & 0 \\ \frac{s_2c_1}{\sqrt{e}} & 0 & 1 & 0 \\ 0 & 0 & 0 & r \end{pmatrix}. \tag{15}$$

Using Eq. (15), the determinant of the Jacobian matrix was found as:

$$\det(\mathbf{J}) = r\frac{c_2c_1}{\left(s_2^2c_1^2 + c_2^2\right)^{3/2}}. \tag{16}$$

which indicates that the singular points of the mechanism are located at $\theta_1 = \pm\pi/2$ and $\theta_2 = \pm\pi/2$.

In order to further elaborate on the kinematics quality of the mechanism, an isotropy index was calculated. The condition number, defined in Eq. (17), was selected as the measure of isotropy.

$$\kappa = \frac{\sigma_{\max}}{\sigma_{\min}}, \tag{17}$$

where $\sigma_{\max}$ and $\sigma_{\min}$ are the largest and smallest singular values of the Jacobian matrix in a particular position. Considering Eq. (16), there is a constant singular point in the mechanism at $r = 0$, which is independent of the mechanism's configuration. Thus, the condition number of the mechanism within its workspace is in fact a function of variations of $q_1$ and $q_2$ over the workspace.

### *2.3. Design synthesis*

The main design parameters of the mechanism are shown in Figure 3. In this figure, $l_1$, $l_2$, $l_3$, and $l_4$ are the dimensions of the gimbal arms and $l_5$ is the length of the tool shaft. In order to appropriately select these dimensions, the main requirement is covering the desired workspace (Figure 1) with no collision between the components. On the other hand, the moving parts of the mechanism should have a small floating inertia. Therefore, it is desirable to find the smallest possible dimensions for the links of the mechanism that provide the required collision-free workspace. Note that other design requirements, such as kinematic performance indices, are independent of the link lengths in spherical mechanisms.

In order to achieve the above aim, a heuristic approach was used in our study. A cost function (Eq. (18)) is defined to minimize the links' dimensions while observing the resulting workspace to ensure that it matches the desired space with no collision.

$$C(l_1, l_2, l_3, l_4, l_5) = \begin{cases} \infty & \text{if the collision free} \\ & \text{workspace is not covered} \\ w_1\frac{l_1}{l_1^*} + w_2\frac{l_2}{l_2^*} + w_3\frac{l_3}{l_3^*} & \\ \quad + w_4\frac{l_4}{l_4^*} + w_5\frac{l_5}{l_5^*} & \text{otherwise} \end{cases} \tag{18}$$

In this equation, $C$ represents the cost function, and $w_i$ stands for the weight factor of each dimension, assumed equal in our analysis. Also, $l_i^*$ and $l_i$ are the initial and the optimized lengths of the $i$th link, respectively.

In the next step, the dynamics of the mechanism are investigated to size the actuators of the robot. For each DOF, the output torque of the actuator needs to counteract the effects of gravity, inertia, and the external force/moment applied. Considering the fact that surgeons usually move the tool slowly, i.e., with low accelerations and velocities, in real laparoscopic surgeries, it is reasonable to assume the inertial torques to be negligible. Therefore, the main parameters affecting the size of actuators are the weights and the external payloads.

In order to reduce the impact of the weights of the robot components on the size of the actuators, a partial static balancing was attempted so that the weights of the moving components are counterbalanced by the internal forces rather than the actuators' effort. The axes of the four DOFs of the mechanism, i.e., yaw, pitch, roll, and insertion, always pass through a fixed center of rotation at the middle of the gimbal. Thus, we tried to achieve static balancing by locating the mechanism's center of mass at this stationary point. Considering the fact that the roll and linear motion actuators constitute the major moving mass of the mechanism, they were mounted against each other symmetrical to the fixed center. This configuration, as illustrated in Figure 3, helped to locate their center of mass close to the fixed center of the mechanism.

In order to map the external payload onto the actuators of pitch, yaw, and roll motions, a static analysis was performed using the Jacobian of the mechanism. The actuators of the linear and grasping motions were exempted from mapping, considering the fact that these motions were decoupled and their corresponding torques could be calculated directly. The actuator torques of pitch, yaw, and roll motions are estimated by applying the maximum desired moments on the tool handle (Eq. (19)) and using the reduced transpose of the Jacobian matrix (Eq. (20)):

$$\vec{\mathbf{t}}_q = \mathbf{J}_{3\times 3}^T \vec{\mathbf{t}}_e, \tag{19}$$

$$\mathbf{J}_{3\times 3}^T = \begin{pmatrix} \frac{c_3 c_2}{\sqrt{e}} - \frac{s_1 s_2 s_3 c_2}{e} & -\frac{s_3 c_2}{\sqrt{e}} - \frac{c_3 c_2 s_1 s_2}{e} & \frac{s_2 c_1}{\sqrt{e}} \\ \frac{s_3 c_1}{e} & \frac{c_3 c_1}{e} & 0 \\ 0 & 0 & 1 \end{pmatrix}. \tag{20}$$

In these equations, $\vec{\mathbf{t}}_e$ is the vector of external moments on the handle, and $\vec{\mathbf{t}}_q$ is the vector of the actuator output torques. Also, $\mathbf{J}_{3\times 3}^T$ is the reduced transpose of the Jacobian matrix, previously obtained as Eq. (15). As seen from the third row of the reduced transposed Jacobian matrix (Eq. (20)), the roll actuator torque is independent of those of other motions, as expected. However, it does affect the pitch actuator output, as seen in the second row.

Using a rough estimation of the actuators' weights and the design requirements (Table 1), it was estimated that, with the designed counterbalanced configuration, gravity consumed less than 5% of the total actuator output torques. Thus, the desired moments on the tool handle were increased by 5% to obtain the external torque for each DOF. This estimation provided the required torque capacity of the roll actuator which was independent of the tool's position. For finding the pitch and yaw torques, the desired workspace was scanned by moving the tool with a constant step size of one degree. At each step, the external desired moment was applied to the tool handle, and the torques at the pitch and yaw DOFs were obtained. The required torque capacity for each of the pitch and yaw actuators was then determined as the relevant maximum torque found within the robot's workspace.

Considering the relatively large torque capacities needed for the pitch, yaw, and roll actuators of the robot, there were two options; using sufficiently high-capacity large actuators or employing transmissions. We preferred using cable-driven transmissions in order to reduce the actuators' inertial effects. Furthermore, cable drives provide lower friction, back drivability, and zero backlash, all having great importance for the force-transparency of a haptic device. Nevertheless, appropriate capstans and cable preloading have to be incorporated in order to eliminate the cable slippage.

### *2.4. Experimental evaluation*

A fully functional prototype of the robot was fabricated (Figure 5), based on the results of the design synthesis process, e.g., optimal link dimensions, actuators' torque and configuration, and transmission mechanism, to evaluate the efficacy of the designed mechanism experimentally. An optical stereoscopic vision system (MicronTrackers, Claron Technology Inc., Ontario, Canada) was used as an external observer to track the robot's end-effector, i.e., the tool's tip, in real-time. In the setup shown in Figure 6, the 3D camera (Figure 6(a)) detects a set of markers attached to the moving tool's tip, to find the position and orientation of the tool's tip with respect to a fixed Cartesian coordinate system, defined using another set of markers attached to the frame (Figure 6(b)).

In the experimental tests, at first, the workspace of the robot was measured by moving its handle in different directions to the end of the moving range and recording the tool's tip position with the optical tracker. In the next stage, motion planning and tracking experiments were performed to verify the robot's kinematical model and assess its efficacy against the

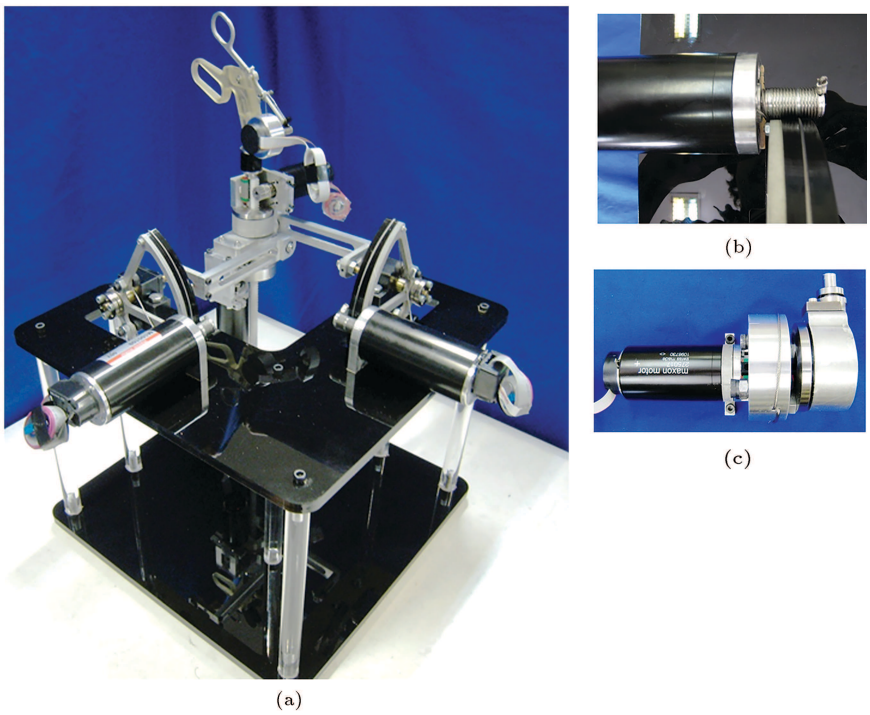


**Figure 5.** The prototype of the robot, including: (a) the main structure, (b) the cable-driven transmission of the pitch actuator, and (c) the cable-drive transmission of the roll actuator.

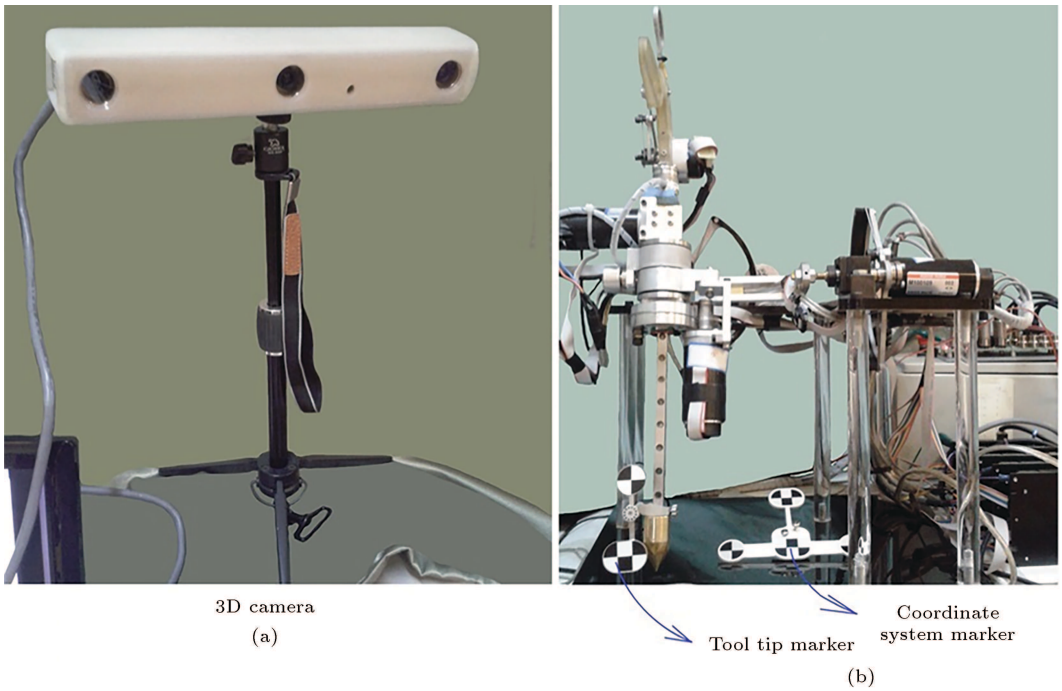


**Figure 6.** The setup of the experimental tests including: (a) a 3D camera and (b) two tracking markers attached to the robot tip and the base.

friction and backlash effects, raised by a relatively large payload. In each test, a desired trajectory, e.g., an offset circle, was defined for the tool's tip to be followed, while it was subjected to a 1 kg hanging weight. The corresponding joint trajectory for each actuator was computed, using the inverse kinematics equations, to generate the position data of the actuators in a simple independent-joint PID tracking control scheme. During each test, the actual joint trajectory for each actuator was measured by recording the position from the encoders, and the resulting trajectory of the tool's tip using the optical 3D tracker.

## 3. Results

The optimized dimensions of the links of the mechanism, obtained by minimizing the cost function of Eq. (18), are indicated in Table 2. The resulting workspace of the robot, found by solving the forward kinematics equations (Eq. (8)), completely covered the desired workspace (Figure 1). Also, the singular points of the mechanism, i.e., $\theta_1 = \pm\pi/2$ and $\theta_2 = \pm\pi/2$, were located outside of the workspace.

The condition number of the robot is illustrated in Figure 7 for variations of $q_1$ and $q_2$ over the workspace, while $q_3$ is assumed to be fixed at zero degrees. The maximum condition number observed for the mechanism was about 2, occurring at the boundaries of $q_1$ and $q_2$. However, it dropped rapidly to values close to one, when moving towards the center of the workspace. These results indicate that the mechanism is highly isotropic in the middle and acceptably isotropic in the peripheral areas of the workspace.

The results of our analysis for finding the required torque capacities of the pitch and yaw actuators are shown in Figure 8(a) and (b), respectively. In this figure, the surface of the maximum torque in the reachable domain of $q_1$ and $q_2$ is illustrated for five different angles of $q_3$. Each surface corresponds to a particular amount of $q_3$ that covers the range of motion by a step size of 45 degrees. The maximum observed torques for yaw and pitch actuators were 8.2 Nm and 8.4 Nm, respectively. For grasping, insertion, and roll actuators, the estimated maximum torques, which were independent of the mechanism's configuration, were found as 0.06 Nm, 0.21 Nm, and 1.05 Nm, respectively.

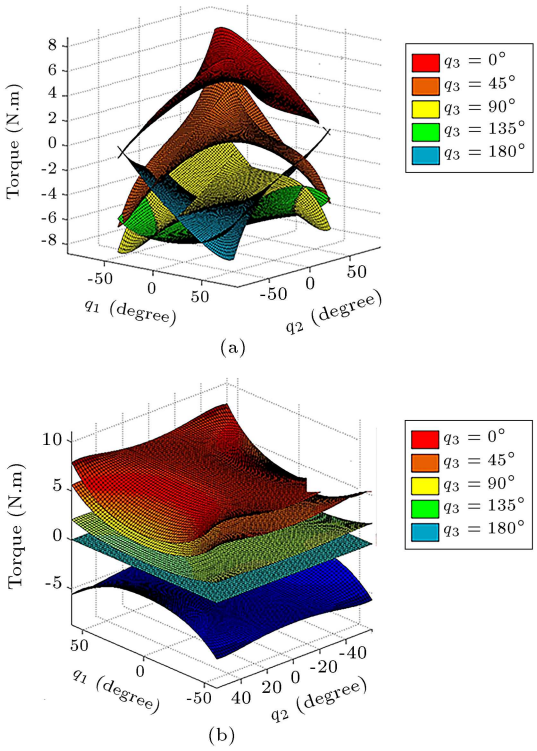


**Figure 8.** The torques of the (a) pitch and (b) yaw actuators at five angles of $q_3$.

**Table 2.** The initial and optimal lengths of the links of the mechanism.

| Link | Initial length (mm) | Optimized length (mm) |
|---|---|---|
| $l_1, l_3$ | 141 | 135 |
| $l_2, l_4$ | 63 | 50 |
| $l_5$ | 300 | 300 |

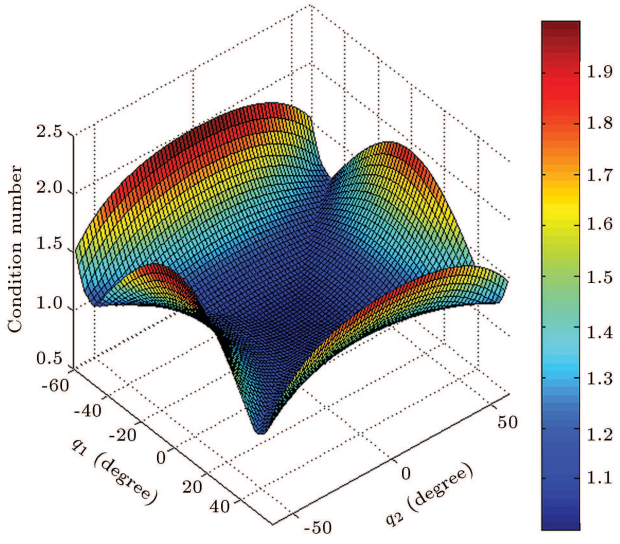


**Figure 7.** The condition number of the mechanism over the workspace.

The details of the functional prototype of the robot are illustrated in Figure 5. The links of the mechanism have been made from aluminum alloy and mounted on a Plexiglas frame. The actuators are from Maxon DC Brushed and Brushless motors (Maxon Motor AG, Switzerland). A rack and pinion mechanism has been utilized to provide the linear motion of the handle which mimics the tool's insertion DOF. The actuators of other DOFs, i.e., grasping, pitch, yaw, and roll, have been coupled to the joints through cable derive transmissions. Figure 5(b) and (c) show the implementation of the cable derive transmission to the landed actuator of the pitch and yaw DOFs, and that of the roll motion, respectively. Two separate strands of flexible aircraft cable have been used, each fixed to a capstan at one end and preloaded at the other, to eliminate slippage of the cable on the capstan. Preloading of strands has been performed using a tension mechanism embedded in the capstans. A similar mechanism has been utilized for the grasping DOF at the tool handle (Figure 9). As illustrated in Figure 9, a six-axis force/torque sensor has been

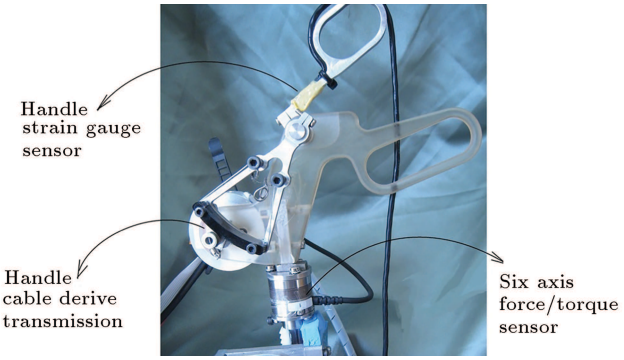


**Figure 9.** The assembly of the handle of the robot. The six DOF force/moment sensor is also shown in the figure.

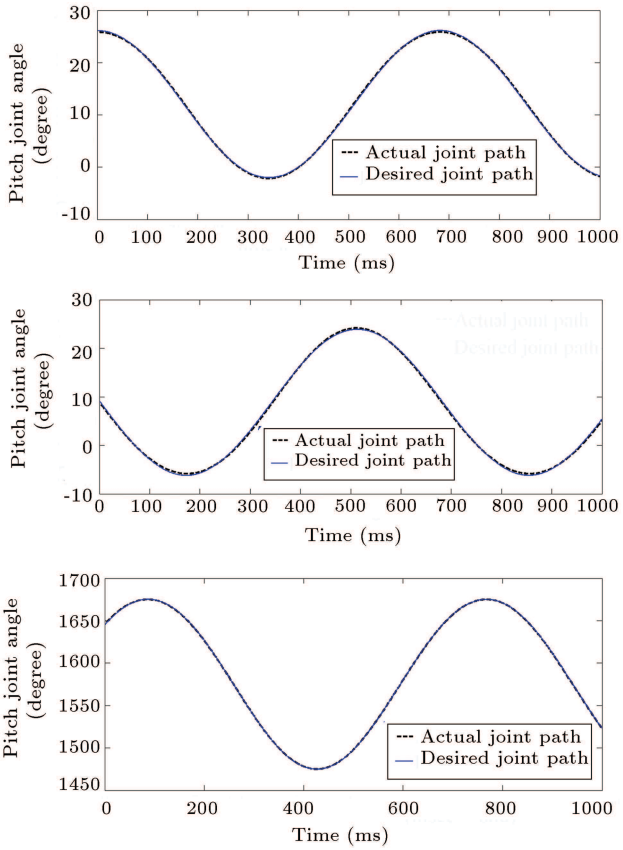


**Figure 10.** The desired and actual trajectories of the pitch, yaw, and insertion joint angles.

also installed between the tool handle and the tool shaft, and a strain gauge sensor on the finger holder, to provide the force/torque feedback for closed-loop control of the robot in the future.

The results of the experimental tests on the prototype of the robot revealed that the desired workspace, defined in Figure 1, is entirely covered by the robot's end-effector, i.e., the tool's tip. The results of the motion planning and tracking experiments for an offset circle, defined as the desired trajectory of the tool's tip, are illustrated in Figures 10 and 11. Three actuators of

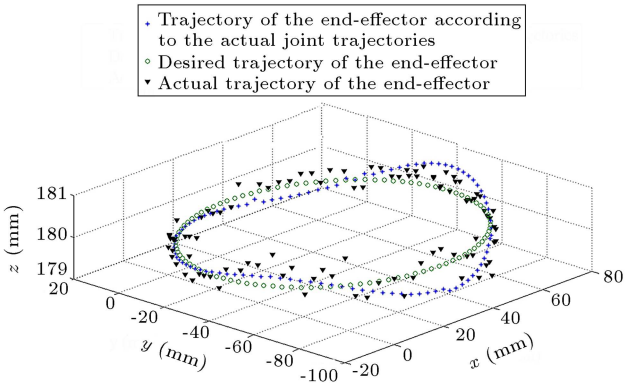


**Figure 11.** The actual trajectory of the end-effector (affected by both controller and mechanics errors), in comparison with the control trajectory (affected only by the kinematic model imperfections) and the desired trajectory. The control trajectory was calculated by applying forward kinematics equations to the plugging actual trajectories of the joints.

the robot, i.e., yaw, pitch, and insertion, were involved in this test, with the desired joint trajectories, calculated from the inverse kinematics, shown in Figure 10 by continuous lines. The actual joint trajectories, measured by the encoders, are also shown in these figures by dashed lines. The maximum recorded errors of trajectory tracking at the joint level were 0.3, 0.4, and 1.8 degrees, respectively, for the pitch, yaw, and insertion DOFs. The resulting calculated trajectory of the tool's tip, obtained by replacing the joints' actual trajectories in the forward kinematics equations of the mechanism, is called the control trajectory and is compared with the desired trajectory in Figure 11. The control trajectory of the tool's tip, as defined above, provides the trajectory that would happen on the tool's tip if the kinematic model of the robot is perfect. Any inaccuracy in the kinematic model would result in a control trajectory that is different from the actual tool's tip trajectory. The maximum observed deviation between the two trajectories was 2.0 mm with an Root Mean Square (RMS) of 0.9 mm. The actual tool's tip trajectory, measured by the 3D optical tracker, is also shown in Figure 11. The maximum and RMS of spatial deviation of the actual trajectory were 2.8 mm and 1.8 mm, from the desired trajectory.

## 4. Discussion

The risks and complexities involved in the laparoscopic manipulation of delicate large intra-abdominal organs have motivated much engineering research in recent years. Most of these investigations have been concerned with developing more sophisticated and effective designs for large-organ laparoscopic instruments [3,4,21,23,24]. However, the development of specially designed surgical simulation systems, that help improve

the surgeons' dexterity during large organ laparoscopic surgery, has been also attempted. Previous investigations in this field mainly targeted improved modeling of the deformation mechanics of large organs [30–34], with no work in the literature concerning the design of appropriate robotic interfaces, to the best of our knowledge. As a result, in spite of the great need for large organ laparoscopic surgery simulation systems, they are not yet available, at least in part due to the fact that the existing robotic interfaces do not meet the essential functional requirements. As indicated earlier, the majority of the robotic interfaces of laparoscopic surgery simulators, which have been fabricated so far, have four actuated DOFs and their force/moments capacities are only sufficient for small organ surgeries, e.g. holecystectomy, oophorectomy, endometriosis treatment and nissen fundoplication [1,8,12–14]. In this study, a robotic interface for large organ laparoscopic surgery simulation was designed, based on the previously designed master robot of haptic tele-surgical systems [35], which enjoys five active DOFs with a sufficiently large force/moment production capacity.

The results of the kinematics analysis of the robot, with the optimized link lengths, indicated that the target workspace was fully covered with no singular points inside. The condition number analysis revealed that the mechanism of the robot was highly isotropic in the middle areas of the workspace, with a condition number of about one, and acceptably isotropic in its peripheral areas (Figure 7). These results imply the capability of the robot to perform surgical maneuvers, well up to the vicinity of the workspace borders, which is in agreement with the observations of the experimental tests.

The main purpose of the experimental tests on the prototype of the robot, in addition to verifying the kinematical model, was to assess the efficacy of the proposed mechanical design against the friction and backlash effects, raised by relatively large payloads that occur during functioning. In order to do so, a trajectory tracking experiment was performed in which the robot's kinematics was measured at two levels of joints' trajectory and the tool's tip trajectory, using encoders and a 3D optical tracker, respectively. This allowed us to isolate two different sources of error that affected the tracking performance of the robot, i.e., controller and mechanics. The error in the mechanics affects the accuracy of the kinematic model. Manufacturing faults and inaccuracies in linear and angular dimensions of components, as well as backlashes at the joints, may contribute to an imperfect kinematic model. In order to characterize this error, the control trajectory, as defined in the last section, was compared with the actual one. If the kinematic model was perfect, the control trajectory, which is the result of the actual joint trajectories and the forward kinematic equations, should be identical to the actual trajectory of the tool's tip. As shown in Figure 11, a maximum error of 2.0 mm and RMS of 0.9 mm was observed between the two trajectories.

On the other hand, the final tracking error at the tool's tip has been also attributed to the tracking error of the joint controllers. In order to determine this contribution, the spatial deviation between the actual and desired trajectories of the tool's tip was measured which showed a maximum of 2.8 mm and RMS of 1.8 mm. This error, as stated before, is the total effect of two contributors: controller and mechanics. Now that the share of the mechanics is identified, by subtraction, it can be concluded that the contribution of the joint controllers tracking error on the final tool's tip tracking error has a maximum of less than or equal to 0.8 mm and an RMS of 0.9 mm.

Considering the results reported in previous studies for small-organ haptic devices, these results suggest that the performance of the designed robotic interface is reasonably acceptable. For instance, Hadavnad et al. [36], reported a larger error, with a maximum of 6 mm, for the tracking accuracy of their haptic telesurgery system against a zero payload. Moreover, considering the ultimate function of our robot, for being used in a laparoscopic surgery training system, a 2 mm tracking error seems tolerable, in view of the fact that the accuracy is not as critical as that of the telesurgery. Nevertheless, this was the first prototype of the robot with inevitable manufacturing imperfections, particularly at the joints. Further work is underway to develop a new prototype with improved mechanics, which will be integrated into a large organ surgical simulation system for practical evaluations. Moreover, the dynamic modeling, analysis, and verification of the mechanism, using the approach provided in [37], will be pursued in future studies.

## 5. Conclusion

In this paper a new 5-DOF robotic interface is designed and evaluated for application in large organ laparoscopic surgery haptic simulation. The proposed mechanism provides yaw, pitch, roll, insertion and grasping DOFs by employing a hybrid mechanism containing a modified parallel four-bar linkage integrated with three serial joints in series. Counterbalanced configuration is used for yaw and pitch DOFs and cable-driven transmission is exploited for roll and insertion DOFs to decrease the effects of inertia, backlash and friction. To identify the design parameters, kinematic analysis was applied. The results revealed that the designed mechanism provide the desirable workspace with no singular points. The efficacy of the designed mechanism is evaluated using the optical stereoscopic vision system as an external observer of to track the robot's end-

effector to follow a desired trajectory in real time while it is subjected to a 1 kg hanging weight. According to the experimental results, the error between the desired and real trajectories had a maximum error of 2.0 mm and RMS of 0.9 mm. It can be concluded from the results that the presented mechanism can be effectively used for laparoscopic surgery training through haptic simulators.

## Acknowledgments

The support of Parseh Intelligent Surgical Systems (Parsiss) in facilitating the experiments is appreciated. This research was funded in part by grant No G005 from Iranian National Science Foundation (INSF).

## Nomenclature

| | |
|---|---|
| $f_{hx}$ | Tool handle force in the $x$ direction |
| $f_{hy}$ | Tool handle force in the $y$ direction |
| $f_{hz}$ | Tool handle force in the $z$ direction |
| $f_{tx}$ | Tool's tip force in the $x$ direction |
| $f_{ty}$ | Tool's tip force in the $y$ direction |
| $f_{tz}$ | Tool's tip force in the $z$ direction |
| $l$ | Displacement of frame 5 along $z_5$ axis from the tool's center of rotation |
| $m_{hz}$ | Torsional moment around the tool handle |
| $m_{hg}$ | Bending moment caused by the thumb's grasping force |
| $m_{tg}$ | Tool's tip gripping moment |
| $m_{tz}$ | Torsional moment around the tool shaft |
| $q_1$ | Actuator 1 angle |
| $q_2$ | Actuator 2 angle |
| $q_3$ | Actuator 3 angle |
| $q_4$ | Actuator 4 angle |
| $q_5$ | Actuator 5 angle |
| $r$ | Actuator 4 pulley radius |
| $(x_p, y_p, z_p)$ | Tool's tip coordinates |
| $\alpha$ | Yaw angle of the $x_3y_3z_3$ coordinate system |
| $\theta_1$ | Pitch angle of the $x_1y_1z_1$ coordinate system |
| $\gamma$ | Roll angle of frame 5 around $z_5$ |
| $\kappa$ | Mechanism condition number |
| $\sigma_{\min}, \sigma_{\max}$ | Minimum and Maximum singular values of the Jacobian matrix |
| $\mathbf{J}(q)$ | Mechanism Jacobian matrix |
| $\mathbf{R}_5^0$ | Rotation matrix from $x_5y_5z_5$ to $x_0y_0z_0$ |
| $\vec{\mathbf{t}}_e$ | Vector of external moments |
| $\vec{\mathbf{t}}_q$ | Vector of actuator moments |
| $\vec{\mathbf{v}}_5^5$ | Tool's tip velocity vector |

## References

1. Hong, M., Rozenblit, J.W., and Hamilton, A.J. "Simulation-based surgical training systems in laparoscopic surgery: A current review", *Virtual Reality*, **25**(2), pp. 491–510 (2021).
2. Heijnsdijk, E.A.M., Dankelman, J., and Gouma, D.J. "Effectiveness of grasping and duration of clamping using laparoscopic graspers", *Surgical Endoscopy and other Interventional Techniques*, **16**(9), pp. 1329–1331 (2002).
3. Mirbagheri, A. and Farahmand, F. "Design, analysis, and experimental evaluation of a novel three-fingered endoscopic large-organ grasper", *Journal of Medical Devices*, **7**(2), 025001 (2013).
4. Amirkhani, G., Farahmand, F.,Yazdian, S.M., et al. "An extended algorithm for autonomous grasping of soft tissues during robotic surgery", *The International Journal of Medical Robotics and Computer Assisted Surgery*, **16**(5), pp. 1–15 (2020).
5. Guo, Y., Cai, C., and Li, W. "Friction behaviour between a laparoscopic grasper and the large intestine during minimally invasive surgery", *Biosurface and Biotribology*, **8**(1), pp. 58–68 (2022).
6. Sun, K., Li, M., Wang, S., et al. "Development of a fiber Bragg grating-enabled clamping force sensor integrated on a grasper for laparoscopic surgery", *IEEE Sensors Journal*, **21**(15), pp. 16681–16690 (2021).
7. Bhakhri, K., Harrison-Phipps, K., Harling, L., et al. "Should robotic surgery simulation be introduced in the core surgical training curriculum?", *Frontiers in Surgery*, **8**, 595203 (2021).
8. Badash, I., Burtt, K., Solorzano, C.A., et al. "Innovations in surgery simulation: a review of past, current and future techniques", *Annals of Translational Medicine*, **4**(23) (2016).
9. Sadeghnejad, S., Elyasi, N., Farahmand, F., et al. "Hyperelastic modeling of sino-nasal tissue for haptic neurosurgery simulation", *Scientia Iranica*, **27**(3), pp. 1266–1276 (2020).
10. Silva, A.J., Ramirez, O.A.D., Vega, V.P., et al. "Phantom omni haptic device: Kinematic and manipulability", *2009 Electronics, Robotics and Automotive Mechanics Conference (CERMA)*, Morelos, Mexico, pp. 193–198 (2009).
11. Lelevé, A., McDaniel, T., and Rossa, C. "Haptic training simulation", *Frontiers in Virtual Reality*, **1**, p. 3 (2020).
12. Payandeh, S. and Li, "Toward new designs of haptic devices for minimally invasive surgery", *International Congress Series*, **1256**, pp. 775–781 (2003).

13. Basafa, E., Sheikholeslami, M., Mirbagheri, A., et al. "Design and implementation of series elastic actuators for a haptic laparoscopic device", *2009 Annu. Int. Conf. IEEE Eng. Med. Biol.*, pp. 6054–6057 (2009).

14. Khan, Z.A., Kamal, N., Hameed, A., et al. "SmartSIM-a virtual reality simulator for laparoscopy training using a generic physics engine", *Int. J. Med. Robot. Comput. Assist. Surg.*, **13**(3), p. e1771 (2017).

15. "CAE LapVR, CAE Healthcare", https://www.caehealthcare.com/surgical-simulation/lapvr/, cited July 16 (2021).

16. "LapSim, surgical science", https://surgicalscience.com/simulators/lapsim/, cited July 16 (2021).

17. Dalvand, M.M., Nahavandi, S., Fielding, M., et al. "Modular instrument for a haptically-enabled robotic surgical system (herosurg)", *IEEE Access*, **6**, pp. 31974–31982 (2018).

18. Wang, P., Zhang, S., Liu, Z., et al. "Smart laparoscopic grasper integrated with fiber Bragg grating based tactile sensor for real-time force feedback", *Journal of Biophotonics*, **15**(5), e202100331 (2022).

19. Sata, N., Shiozawa, M., Suzuki, A., et al. "Retroperitoneal hand-assisted laparoscopic surgery for endoscopic adrenalectomy", *Surg. Endosc. Other Interv. Tech.*, **20**(5), pp. 830–833 (2006).

20. Habermalz, B., Sauerland, S., Decker, G., et al. "Laparoscopic splenectomy: the clinical practice guidelines of the European Association for Endoscopic Surgery (EAES)", *Surgical Endoscopy*, **22**(4), pp. 821–848 (2008).

21. Mirbagheri, A. and Farahmand, F. "A triple-jaw actuated and sensorized instrument for grasping large organs during minimally invasive robotic surgery", *Int. J. Med. Robot. Comput. Assist. Surg.*, **9**(1), pp. 83–93 (2013).

22. Liu, H., Selvaggio, M., Ferrentino, P., et al. "The MUSHA hand II: A multifunctional hand for robot-assisted laparoscopic surgery", *IEEE/ASME Trans. Mechatron.*, **26**(1), pp. 393–404 (2020).

23. Khadem, S.M., Behzadipour, S., Boroushaki, M., et al. "Design and implementation of an emotional learning controller for force control of a robotic laparoscopic instrument", *Frontiers in Biomedical Technologies*, **1**(3), pp. 168–181 (2014).

24. Khadem, S.M., Behzadipour, S., Mirbagheri, A., et al. "A modular force-controlled robotic instrument for minimally invasive surgery-efficacy for being used in autonomous grasping against a variable pull force", *Int. J. Med. Robot. Comput. Assist. Surg.*, **12**(4), pp. 620–633 (2016).

25. Waters, I., Wang, L., Jones, D., et al. "Incipient slip sensing for improved grasping in robot assisted surgery", *IEEE Sensors Journal*, **22**(16), pp. 16545–16554 (2022).

26. Waters, I., Jones, D., Alazmani, A., et al. "Utilising incipient slip for grasping automation in robot assisted surgery", *IEEE Robot. Autom. Lett.*, **7**(2), pp. 1071–1078 (2021).

27. Lum, M.J., Rosen, J., Sinanan, M.N., et al. "Optimization of a spherical mechanism for a minimally invasive surgical robot: theoretical and experimental approaches", *IEEE Trans. Biomed. Eng.*, **53**(7), pp. 1440–1445 (2006).

28. Rosen, J., MacFarlane, M., Richards, C., et al. "Surgeon-tool force/torque signatures-evaluation of surgical skills in minimally invasive surgery", *Stud. Health Technol. Inform.*, **62**, pp. 290–296 (1999).

29. Trejos, A.L., Patel, R.V., and Naish, M.D. "Force sensing and its application in minimally invasive surgery and therapy: a survey", *Proceedings of the Institution of Mechanical Engineers, Part C: Journal of Mechanical Engineering Science*, **224**(7), pp. 1435–1454 (2010).

30. Basafa, E., Farahmand, F., and Vossoughi, G. "A nonlinear mass-spring model for more realistic and efficient simulation of soft tissues surgery", *Stud. Health Technol. Inform.*, **132**, p. 23 (2008).

31. Tirehdast, M., Mirbagheri, A., Asghari, M., et al. "Modeling of interaction between a three-fingered surgical grasper and human spleen", In *Medicine Meets Virtual Reality*, **18**, pp. 663–669, IOS Press (2011).

32. Basafa, E. and Farahmand, F. "Real-time simulation of the nonlinear visco-elastic deformations of soft tissues", *Int. J. Comput. Assist. Radiol. Surg.*, **6**(3), pp. 297–307 (2011).

33. Abdi, E., Farahmand, F., and Durali, M. "A meshless EFG-based algorithm for 3D deformable modeling of soft tissue in real-time", *Medicine Meets Virtual Reality*, **19**, pp. 1–7, IOS Press (2012).

34. Dehghani Ashkezari, H., Mirbagheri, A., Behzadipour, S., et al. "A mass-spring-damper model for real time simulation of the frictional grasping interactions between surgical tools and large organs", *Scientia Iranica*, **22**(5), pp. 1833–1841 (2015).

35. Rosenberg, L.B. "Multiple degree-of-freedom mechanical interface to a computer system", U.S. Patent No. 6,246,390, 12 Jun. (2001).

36. Hadavand, M., Mirbagheri, A., Behzadipour, S., et al., "A novel remote center of motion mechanism for the force-reflective master robot of haptic tele-surgery systems", *Int. J. Med. Robot. Comput. Assist. Surg.*, **10**(2), pp. 129–139 (2014).

37. Guan, D., Yang, N., Lai, J., et al. "Kinematic modeling and constraint analysis for robotic excavator operations in piling construction", *Automation in Construction*, **126**, 103666 (2021).

## Biographies

**Hamed Jamshidifar** received a BSc degree from the Isfahan University of Technology, in 2008, an MSc degree from the Sharif University of Technology in

2011, both in mechanical engineering and a PhD degree in mechanical and mechatronics engineering from the University of Waterloo, Waterloo, Canada, in 2018. He is currently a Senior Advanced Systems Engineer with Honeywell, Mississauga, Canada. His research interests include robotics, control and dynamical systems, cable-driven robots, and surgical robotic systems.

**Farzam Farahmand** received an MSc degree in Mechanical Engineering, from the University of Tehran, Tehran, Iran in 1992 and a PhD degree in Biomechanical Engineering from Imperial College of Science, Technology and Medicine, London, UK, in 1996. In 1997, he joined the Mechanical Engineering Department of the Sharif University of Technology, Tehran, Iran, where he is a professor and head of the Biomechanics Division. He has a joint appointment in the Research Center for Biomedical Technologies and Robotics (RCBTR), Tehran University of Medical Sciences, Tehran, Iran. His research is focused on human motion, orthopedic biomechanics, and medical robotics. In his career, he has developed several medical instruments and devices and published numerous journal and conference papers in different fields of biomechanics and biomedical robotics.

**Saeed Behzadipour** received his BSc and MSc in Mechanical Engineering from the Sharif University of Technology, Iran in 1998 and 2000, respectively. He received his PhD in Mechanical Engineering from the University of Waterloo, Canada in 2005. He was an Associate Professor in Mechanical Engineering at the University of Alberta, Canada until 2011. He is now a Professor in the Mechanical Engineering Department, and jointly affiliated with Mowaffaghyian Research Center in Neuro-rehab Technologies at Sharif University of Technology. His research interests include the design and control of medical robotics systems, and rehabilitation engineering.

**Alireza Mirbagheri** received a PhD degree in Mechanical Engineering from the Sharif University of Technology, Tehran, Iran, in 2012. Then, he joined the Department of Medical Physics & Biomedical Engineering at the School of Medicine at Tehran University of Medical Sciences (TUMS), where he is an Associate Professor and deputy of research affairs. He has a joint appointment in the Research Center for Biomedical Technologies and Robotics (RCBTR) at the Advanced Medical Technologies and Equipment Institute (AMTEI) of Tehran University of Medical Sciences, where he is the deputy of research affairs and also director of the Robotic Surgery Lab. (RSL). Nowadays, most of his research is focused on the design and implementation of telerobotic surgical systems and haptic surgical instruments.